ISSN 1330-3651 (Print), ISSN 1848-6339 (Online)
https://doi.org/10.17559/TV-20240601001728
Original scientific paper

Wind Tunnel Investigation and Numerical Simulation of Flow Characteristics Around the Enclosed Railing Steel Box Girder Section

Sai GONG, Xue ZHAO, Shucheng YANG*

Abstract: The rapid development of computational fluid dynamics has facilitated its widespread application in bridge design and wind engineering. This paper employs large eddy simulation (LES) to investigate the impact of non-uniformly distributed closed railings along the span of a bridge on flow characteristics, particularly focusing on a steel box girder section and the mechanism for suppressing vortex-induced vibration (VIV). The study delves into various VIV-related flow parameters such as velocity distribution, evolution of three-dimensional vortex structures, and pressure distribution on the girder surface. The findings reveal that significant negative pressure emerges on the leeward side of the upstream bridge deck when the outer railings are closed, resulting in increased downstream airflow in the spanwise direction and diminished vortex energy downstream. Moreover, it is observed that the negative pressure exerted by the bridge deck leads to significant dissipation of vortices induced from the downstream, consequently reducing VIV amplitude. The vibration suppression mechanisms of the two measures are compared and discussed to explore their potential for application in actual design considerations.

Keywords: arge eddy simulation; computational fluid dynamics; vibration suppression measures; vortex induced vibration; wind tunnel test

1 INTRODUCTION

Steel box girders are extensively utilized in modern bridge construction due to their structural efficiency, versatility, and aesthetic appeal. When wind flows around a steel box girder, vortices can form and periodically detach from the structure. This phenomenon, known as vortex shedding, can result in unwanted vibrations called vortex-induced vibrations (VIV) if the shedding frequency coincides with the natural frequency of the girder. To suppress the potential VIV of a steel box girder, appropriate aerodynamic measures are considered to ensure the safety and performance of long-span bridges subjected to fluctuating wind loads (2 - 3 citations).

Due to the separation and reattachment of the flow field, the aerodynamic performance of the box girder is significantly affected by the auxiliary structural members. For example, the influence of the railing on the vortex-induced vibration performance of the main beam is very significant [1]. The existing optimizations for railings mainly include height, ventilation rate, inclination angle, and railing cornerstone. Wang Yangxue [2] used section model vibration and pressure measurement tests to study the influence of three parameters affecting the shape of the railing, namely, the inclination angle of the railing, the height of the railing and the ventilation rate of the railing, on the vortex vibration performance of the streamlined box. Liu Qingkuan et al. [3] found through wind tunnel tests that when the height of the railing is 45% of the beam height, the vortex amplitude of the streamlined box girder is the largest. On this basis, appropriately reducing or increasing the height of the railing has a certain vibration suppression effect. Through the large-scale section model wind tunnel test, Li Chunguang et al. [4] compared and analyzed the vortex vibration performance of the main beam under three different positions and heights of the railing foundation. The results show that moving the railing foundation to the edge of the bridge deck can effectively suppress the vortex vibration. The impact of the wind penetration rate of the railing on the characteristics of vortex-induced vibrations in the main beam has been studied by Cui Xin et al. [5]. Their research revealed that reducing the penetration rate alters the shedding frequency of vortices, shifting it away from the torsional frequency. As a result, the amplitude of vortex-induced vibrations weakens or their occurrence is suppressed. Similar conclusions were reached by Li Ming et al. [6] in their investigation of optimizing vortex-induced vibration control measures for a long-span suspension bridge. Their experimental study demonstrated that the most effective suppression effect was achieved by incorporating vibration suppression plates of a specific height and wind penetration rate on both sides of the main beam guard rail. Additionally, Cao Fengchan et al. [7]compared wind tunnel test results for both the construction and completed sections of a bridge and determined that the addition of the railing was the primary cause of significant vibrations in the completed state. Inspired by the spanwise sinusoidal perturbation method, Li Ming et al. [10] used wind tunnel tests to verify that the traffic barrier with regular interval sealing plates along the bridge deck can successfully suppress the heave vortex vibration of the box girder. These experimental studies underscored the efficacy of using enclosed railings to mitigate vibrations resulting from vortex shedding. However, the underlying mechanism behind this phenomenon remains unclear, which is one of the research objectives of this study.

Instead of relying on time-consuming and expensive wind tunnel tests, researchers have increasingly turned to numerical simulations using computational fluid dynamics (CFD) in a virtual wind tunnel. CFD simulations offer economic advantages and provide visualized flow fields, thanks to advancements in computer technology. However, achieving accurate calculations in CFD simulations requires careful grid generation and selection of turbulence models. Commonly used turbulence models include Direct Numerical Simulation (DNS) [10], Reynolds-Averaged Navier-Stokes (RANS) models [12-14], and Large Eddy Simulation (LES) methods [15-17]. For example, Zhang Liangliang et al. [18] utilized CFD technology to study the impact of the wind penetration rate of railings on the three force components of a near-streamline wide-box girder. They found that as the wind penetration rate of the railing decreases, the airflow reattaches to the upper surface and

moves downward, resulting in significant differences in aerodynamic force distribution for different angles of attack on the model's surface. Similarly, Jiang Tianhua [19] investigated the influence of different railing forms on static loads using CFD technology. They concluded that a perforated railing also improved the lift coefficient and torque coefficient, with these coefficients decreasing as the penetration rate increased. However, these CFD simulations overlooked the influence of flow characteristics of the steel box girder on its vibration, specifically considering the varying wind penetration rates of the railings.

The steel box girder section exhibits significant bluff body characteristics and is prone to vortex-induced vibration. To provide essential information on the use of enclosed railings as an aerodynamic measure to mitigate vibrations, the objectives of this study are to investigate the overall flow field of the structure using CFD simulation technology and to analyze the mechanism of vibration initiation in this typical design cross-section. Specifically, a wind tunnel testing program is designed and conducted to measure the structural responses, such as the amplitude of VIV, of the selected steel box girder. The numerical modeling utilizes LES technology, and a transient analysis is performed to capture the synchronized evolution of flow field points. The study investigates various aspects, including velocity distribution in the flow field, the development and evolution of three-dimensional vortices, and the surface pressure distribution on the main beam. Additionally, the flow field characteristics and their impact on structural response are assessed by considering different configurations of wind fences on the railings.

2 WIND TUNNEL INVESTIGATION

The wind tunnel test was carried out in the Boundary Layer Wind Tunnel at Chang'an University (citation?) with the dimension of 3.0 m width, 2.5 m height and 15.0 m length for the test.

2.1 Test Model

The main beam cross-section of a steel box girder with a width-to-height ratio of B/H = 9.7 is selected for the investigation in this study. The standard cross-section of the main beam is shown in Fig. 1.

Table 1 Main parameters of tested model

Parameter	Unit	Scale ratio	Model design value	Model measured values	Inaccuracy / %
Equivalent mass	kg/m	1/202	87.50	86.67	0.95
Equivalent mass	kg×m^2/m	1/204	22.69	/	/
Vertical bending frequency	Hz	20/2	3.37	3.38	0.30
Torsional frequency	Hz	20/2	10.21	10.15	0.59
Vertical bending damping ratio	/	/	/	0.0036	/
Torsional damping ratio	/	/	/	0.0033	/

According to the similarity criterion, considering the size of the wind tunnel test section, a large-scale section model with a length of 1.5 m and a scale ratio of 1:20 is designed. The basic parameters are shown in Tab. 1, and the test model is shown in Fig. 2.

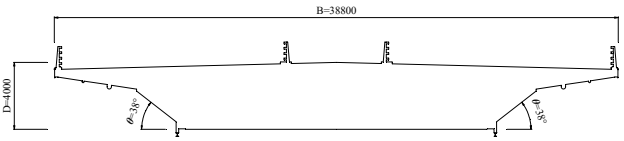

Figure 1 Standard cross-section of the main beam (unit: mm)

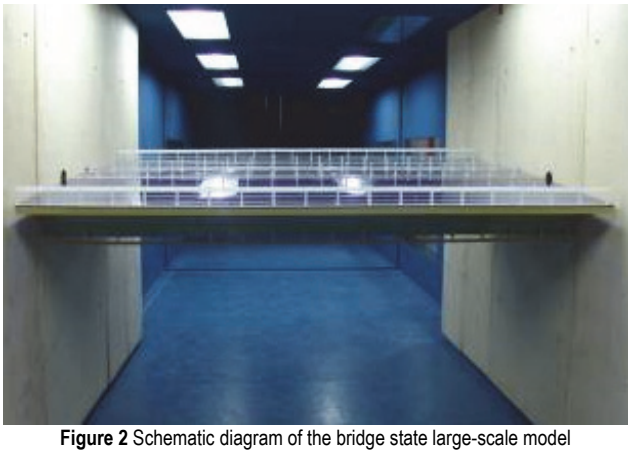

Figure 2 Schematic diagram of the bridge state large-scale model

2.2 Test Results

For the wind tunnel test, the range of wind speed from 2.5 m/s to 25 m/s was used with uniform wind flow.

As shown in Fig. 3, B is the characteristic size, the width of the bridge deck is taken, f_b is the vertical bending frequency of the structure, and U is the converted wind speed of the real bridge.

The section of the main girder of the straight web steel box girder in the bridge state shows vertical vortex-induced vibration, and the vertical bending amplitude is significant at the positive wind attack angle.

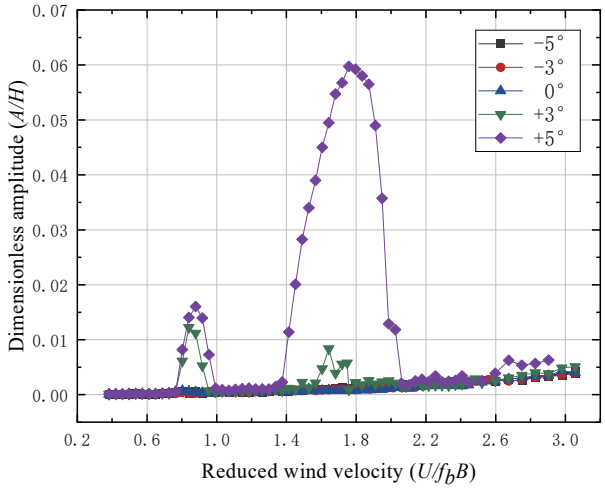

Figure 3 Dimensionless amplitude-wind speed curve of the original section (vertical bending vortex vibration)

To examine the effects of the enclosed railing on the flow field surrounding the steel box girder, two typical vibration suppression measures are explored in this study. The first measure encompasses 2.5 m per 10 m of the railings, designated as measure $M1$, as depicted in Fig. 4a. The second measure encompasses 2.5 m per 7.5 m of the railings, designated as measure $M2$, as depicted in Fig. 4b.

The two aerodynamic measures have obvious inhibitory effect on the vertical bending vibration of the straight web steel box girder section, but the F1K2 arrangement of the outer railing can suppress the small torsion of the original section, and the effect is better. For space reasons, only the test results of the F1K2 arrangement of the outer railings are shown, as shown in Fig. 5.

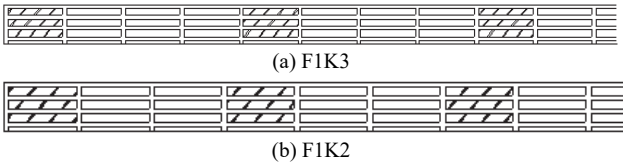

(a) F1K3

(b) F1K2

Figure 4 Schematic diagram of the transverse arrangement of exterior barriers a) F1K3; b) F1K2

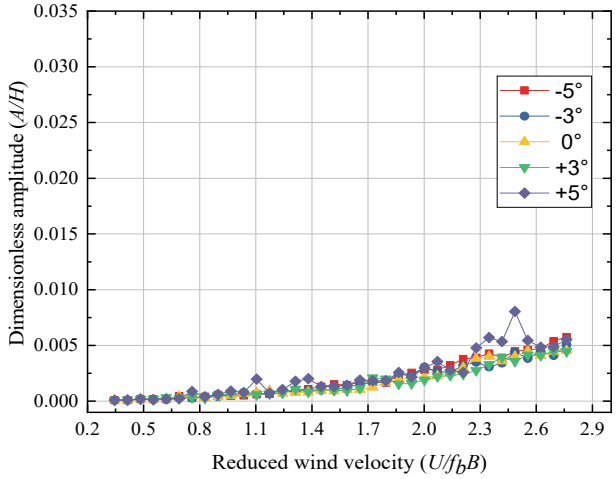

Figure 5 Dimensionless amplitude-wind speed curve of F1K2 measure (vertical bending vortex vibration)

3 NUMERICAL SIMULATION USING COMPUTATIONAL FLUID MECHANICS (CFD)

To further investigate the flow characteristics, the steel box girder with enclosed railings is numerically simulated by using computation fluid mechanics (CFD). The transient flow field under the condition of + 5° and + 3° wind attack angle is calculated by numerical simulation. The calculated wind speed is taken as the starting wind speed Ur = 0.768 under the corresponding wind attack angle of the original section during the test. This working condition corresponds to the significant vertical bending vibration observed in the vibration test and the corresponding aerodynamic measures with uneven lateral arrangement of the outer barrier.

3.1 Simulation Methodology

For the numerical modelling, a same scale is used for the section model as the tested wind tunnel model, i.e. the ratio of the dimension of numerical model to actual bridge is 1:20. As for CFD, a computational domain is first established to generate the wind field. Two CFD domain are modelled as follows (ref????): 1). in order to meet the requirements of blocking rate and prevent the influence of end three-dimensional effect, the numerical wind tunnel with dimensions of $6B \times 20B \times L$, where B and L are the width and length of the considered section model, respectively; 2). in order to control the number of grids while encrypting the grids around the flow field, a small wind field with a diameter of $2B$ is set up. The spanwise size is the same as that of the large wind field, and the shape is set to be cylindrical to facilitate the adjustment of the wind attack angle. The two-dimensional view of the modelled space is shown in Fig. 6. For the simulation, it is assumed that the velocity profile and other properties are consistent with the expected flow behavior at the boundary, and it is assumed that the flow is fully developed and there are no significant pressure gradients normal to the outflow boundary. Therefore, a velocity-inlet boundary condition, which allows the fluid to flow freely into the domain while considering the interaction with the surrounding flow field, is applied. To define the inflow conditions, the turbulence intensity at the velocity inlet is set at 0.5%, and the viscosity ratio is 5%. The Pressure-outflow is used for the outlet, the pressure is determined by the flow solution inside the computational domain, ensuring that the flow exits smoothly without causing reflections or disturbances. Consider that the flow being simulated exhibits symmetry, a Symmetry boundary consideration is also adopted for the upper (i.e., lower) and front (i.e., rear) boundaries for a reduction in the computational domain size and computational effort. Besides, two individual interfaces are set at the contact surfaces of the two computational domains.

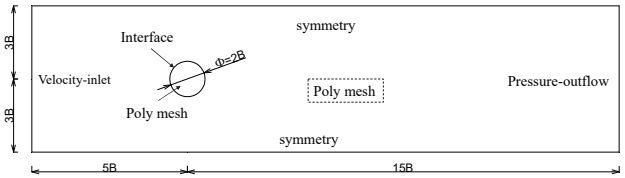

Figure 6 Computational domain settings

3.2 Meshing and Verification

To ensure smooth iteration throughout the numerical wind tunnel flow field, hexahedral meshes are used for meshing with the consideration of its good uniformity. The mesh independence verification results are shown in Tab. 2.

Table 2 Mesh independence verification

Number of Grids	Lift coefficient	Drag coefficient	Pitch moment coefficient
8.0 × 106	1.36	–0.0454	0.1153
6.37 × 106	1.62	–0.0422	0.0977
4.83 × 106	1.77	–0.0415	0.0825
Wind tunnel test	1.489	–0.0474	0.1044

In this study, a mesh quantity of 4.83×10^6 is adopted to analyze the vibration mechanism of the original cross-section and the effectiveness of the uneven transverse arrangement of wind fences. The number of meshes for the simulated wind tunnel computational domain is approximately 100000, for the specified cylinder computational domain is approximately 4.7 million. Fig. 7 shows the schematic diagrams of the computational domain meshes.

The grid quality verification of multiple parameters is performed on the grid. Skewness is the degree to which the mesh is close to the ideal geometry (regular polygon). High

skew rate will reduce the accuracy of the solution and reduce the convergence.

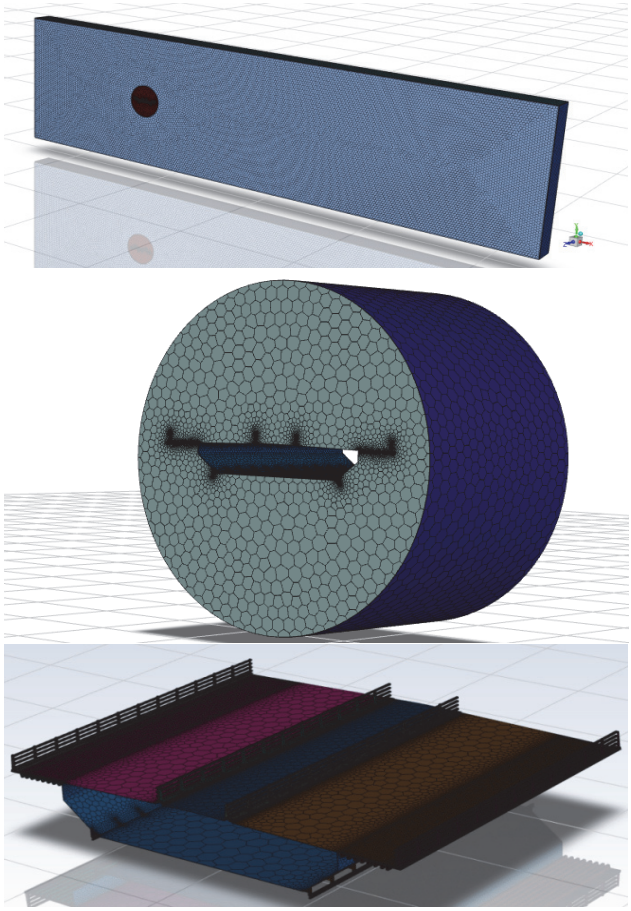

Figure 7 Computational domain meshes: a) The numerical wind tunnel; b) An inside cylindrical domain; c) main girder wall grid.

Therefore, it is required not to be higher than 0.95, preferably below 0.9 and the smaller the better. The aspect ratio is the extent to which the node is elongated, equal to 1 is the best mesh shape, generally less than 5:1, and the requirements can be relaxed near the wall. Squish is used to quantify the non-orthogonality of a mesh relative to its surface. The closer to 0, the better the quality of the mesh. The evaluation results of the quality parameters of the computational domain are shown in Tab. 3, and all parameters meet the requirements of high-quality grids.

Table 3 Mesh quality

Value	Skewness	Aspect Ratio	Squish
Min	0.00165	1.38	0.00134
Max	0.83196	4	0.83196
Evaluation	meet requirement	The length-width ratio near the wall is large (Max 15.7), meet requirement.	meet requirement

3.3 Characteristics of Flow Field

3.3.1 Three-Dimensional Flow Field and Streamwise Distribution

Fig. 8 depicts the isosurface plots of vorticity on the windward side of the selected steel box girder under a +5° wind attack angle, at t = 3T/4 and Q = 1E–03, for the original cross-section and the F1K2 configuration. It is indicated from the CFD results that the railings are arranged in the F1K2 configuration, the flow is blocked in front of the railings, preventing the formation of vortices on the windward side. Additionally, the collision between the flow and the railings alters the flow direction upstream, resulting in larger vortices above the closed section for the same threshold criterion Q, as indicated by the black box in Fig. 9. The pressure is relatively lower on the downstream side of the closed section compared to the open sections on both sides, causing the airflow from both sides to be drawn into this region. As a result, vortices are formed at the outer columns on the side of the closed section, rotating around the Y-axis, as shown in the red frame of Fig. 8. The distinct vortex structure near the central crash barrier of the original cross-section disappears at the same time step.

It can be observed that uneven arrangement of the railings enhances the three-dimensional vortex complexity in the flow field. Assuming the inflow has the same energy input to the structure and its surrounding flow field, implementing uneven arrangement of the external railings leads to two main changes in the flow field: 1) The inflow on the windward side of the closed section is hindered, resulting in a decrease in fluid kinetic energy; 2) From the perspective of vortex structure, under the negative pressure on the downstream side of the closed section, the velocity component in the streamwise direction increases, and vortices rotating around the Y-axis become evident. This, in turn, reduces the energy of the upstream vortices responsible for the vertical vibration of the main beam across the entire bridge deck when the wind penetration rate is the same.

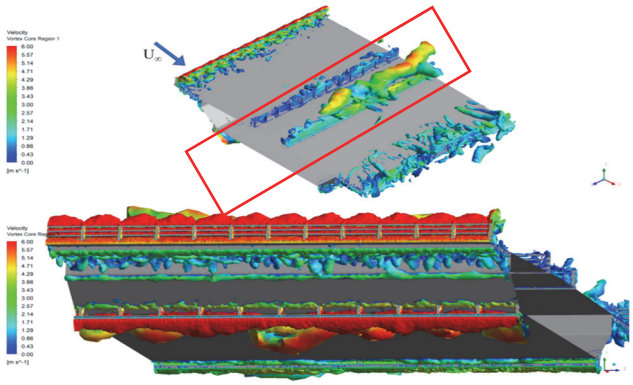

Figure 8 Distribution of vortex velocity on the upper and side surfaces of the original cross-section (t = 3T/4, Q = 1E–03)

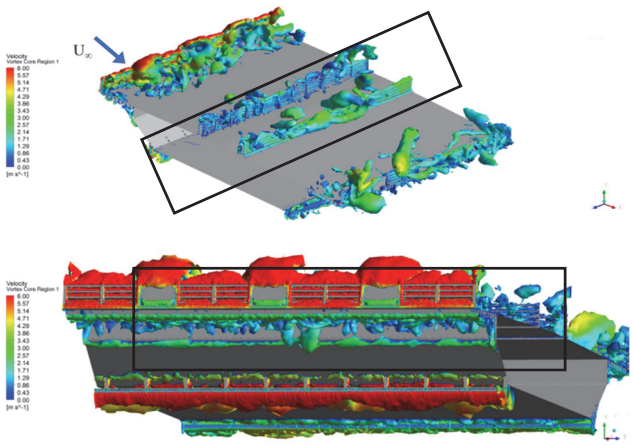

Figure 9 Distribution of vortex velocity on the upper and side surfaces of the F1K2 configuration (t = 3T/4, Q = 1E–03)

In the wake region of the model, at a height located halfway between the main beam height, along the wind direction, at distances of 0.2*B*, 0.4*B*, 0.6*B*, 0.8*B*, 1*B*, 2*B*, and 3*B* from the outermost downstream point of the model, seven rows of measurement points are arranged. Each row consists of 45 measurement points. By comparing the vorticity of the original cross-section with the vorticity of the cross-section with added aerodynamic measures in Fig. 10 to Fig. 13, it can be observed that the spanwise spacing closure of the railings increases the vorticity in the *X* and *Y* directions. In Fig. 13, it is indicated that the maximum value of the vorticity in the *Z* direction decreases, and a change in the rotation direction of the vortices occurs in the spanwise direction, enhancing the three-dimensional non-uniformity of the flow field.

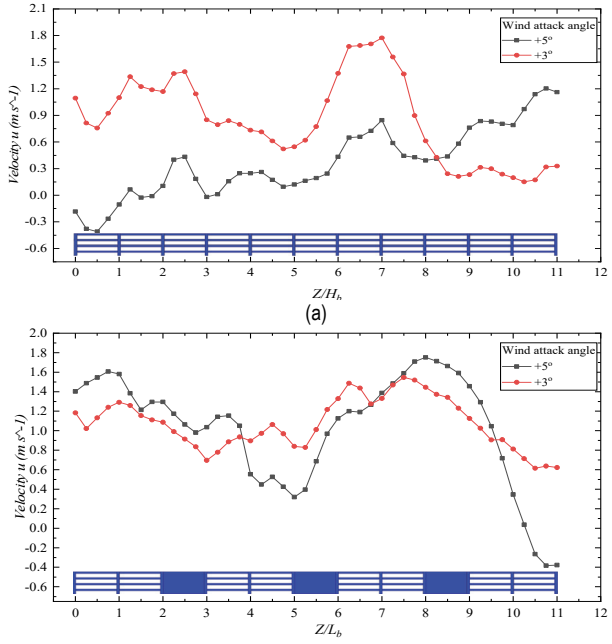

Figure 10 Horizontal distribution of wind speed: a). No wind fences; b) With wind fences arrangement F1K2

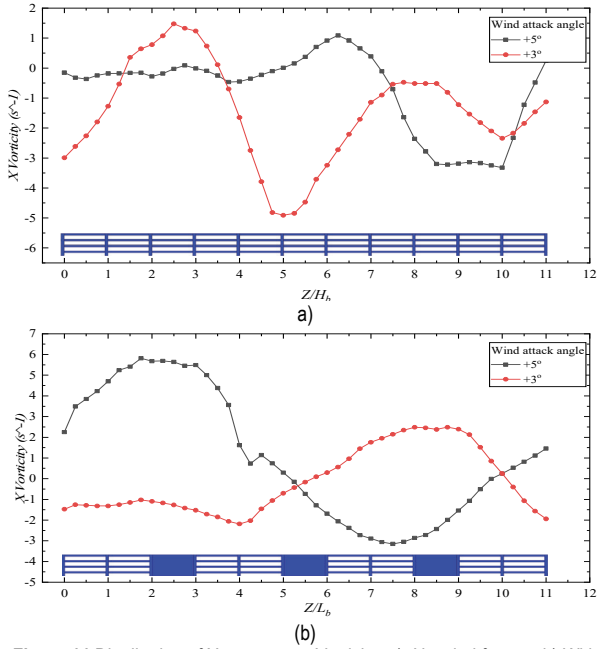

Figure 11 Distribution of X-component Vorticity: a). No wind fences; b) With wind fences arrangement F1K2

As shown in Fig. 11b within the red box, for the vortices rotating around the *X*-axis, a change in the vorticity direction occurs at *Z*/*Lb* = 5 in the wake region near the structural position for both wind attack angles after the closure of the railings. The vortices on both sides rotate in opposite directions around the *X*-axis, and their magnitudes of vorticity are similar. According to Fig. 12, for the vortices rotating around the *Y*-axis, the trend of vorticity change in the wake region is similar before and after the addition of aerodynamic measures, but the vorticity significantly increases. Therefore, when the energy components of the wake vortices in the *X* and *Y* directions are enhanced, under the condition of the same upstream wind speed, the distribution of vortex energy in the downstream direction is reduced, which can suppress the vibration of the main beam.

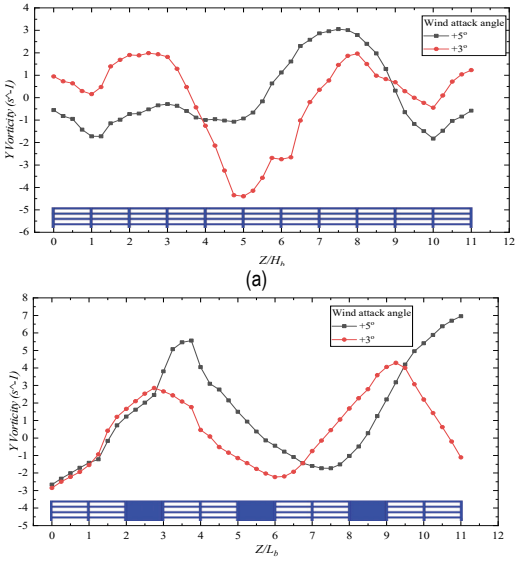

Figure 12 Distribution of Y-component Vorticity: a). No wind fences; b) With wind fences arrangement F1K2

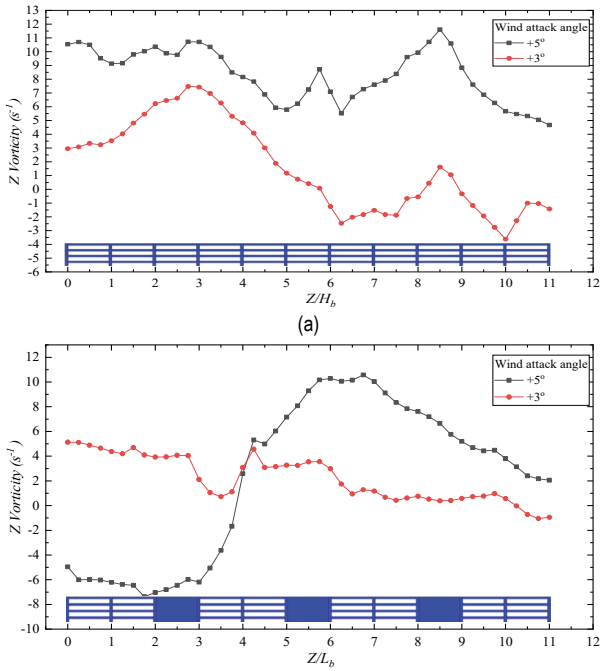

Figure 13 Distribution of Z-component Vorticity: a). No wind fences; b) F1K2 cross-section

3.3.2 Velocity and Vorticity Evolution

To further investigate the impact of the enclosed railings on the flow behaviour, a slice of the central section (ZX) of the mid-span is extracted from the available data points. The transient streamline diagrams of the original ZX cross-section and the F1K2 ZX cross-section at a +5° wind angle of attack are contoured and presented in Fig. 14 to Fig. 17.

The ZX cross-section features fully enclosed outer barriers on both sides of the main beam, with only a transverse bar at the central crash barrier. From Fig. 14 and Fig. 15, it is shown that at the moments $T/4$ and $2T/4$, the vortex structure within the black frame undergoes changes after passing through the non-uniform closed barriers. The large vortices are dispersed, forming smaller vortices, and their quantity decreases. The vortex structure within the black frame undergoes changes when it passes through non-uniform closed barriers. The larger vortices disperse and form smaller vortices, resulting in a decrease in their overall quantity.

At the moment of $t = 3T/4$ and $t = T$, the large vortex indicated (shown in the frame in (a) undergoes changes after passing through the non-uniform closed barriers. The vortex is flattened and becomes more wall-attached. In general, compared to the streamline diagram of the original ZX cross-section, the F1K2 measure exhibits a development trend of the main flow direction towards the lower surface of the bridge deck in the upper part of the boundary layer. As a result, it compresses and deforms the vortices within the boundary layer. The height position of the vortices that originally passed over the central crash barrier is lowered due to interference from the transverse bar of the barrier, resulting in a reduction in vortex size. Moreover, the vortices at the downstream bridge deck are more closely attached to the wall, leading to a decrease in rotational speed under the influence of wall friction. This results in a reduced aerodynamic force on the deck.

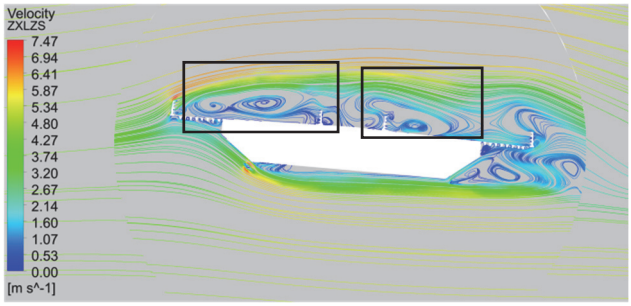

(a)

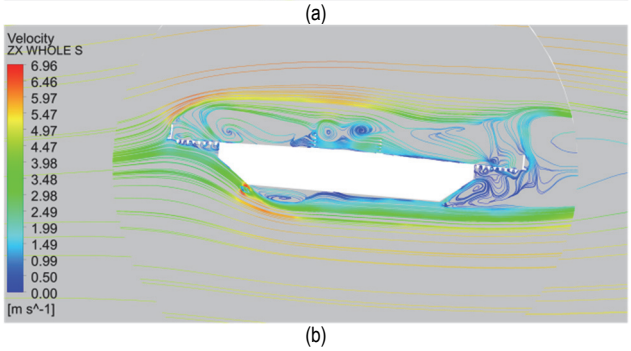

(b)

Figure 14 Instantaneous streamline diagram of $T/4$ for +5° wind attack angle section: a). original-ZX section; b) F1K2-ZX cross-section

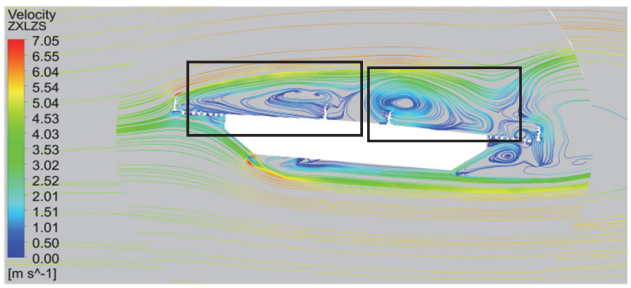

(a)

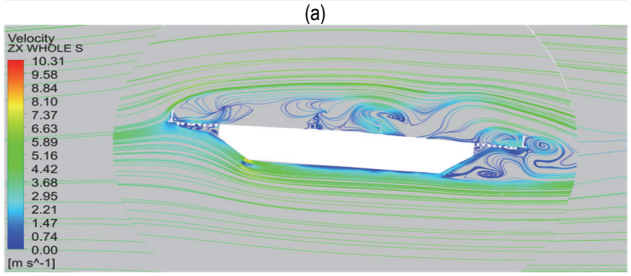

(b)

Figure 15 Instantaneous streamline diagram of 2T/4 for +5° wind attack angle section: a). original-ZX section; b) F1K2-ZX cross-section

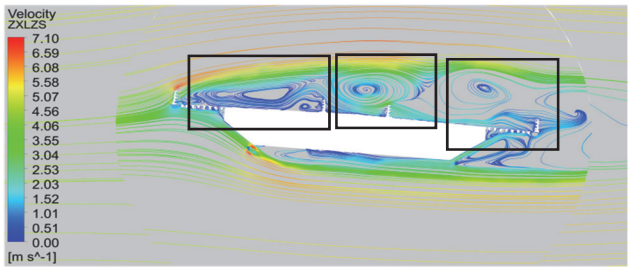

(a)

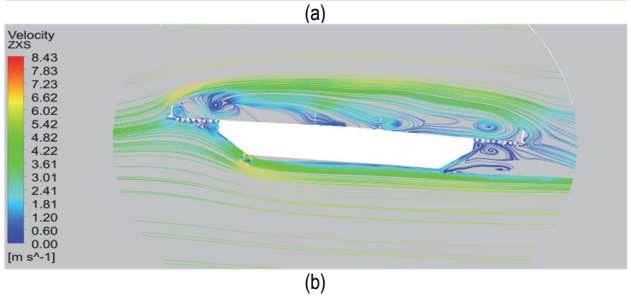

(b)

Figure 16 Instantaneous streamline diagram of 3T/4 for +5° wind attack angle section: a). original-ZX section; b) F1K2-ZX cross-section.

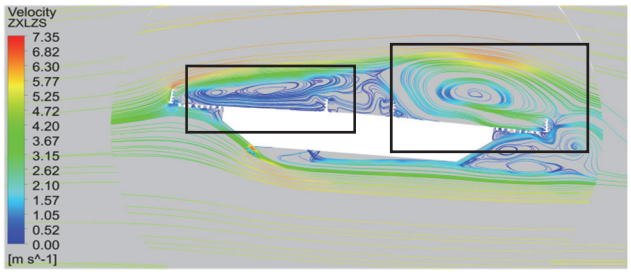

(a)

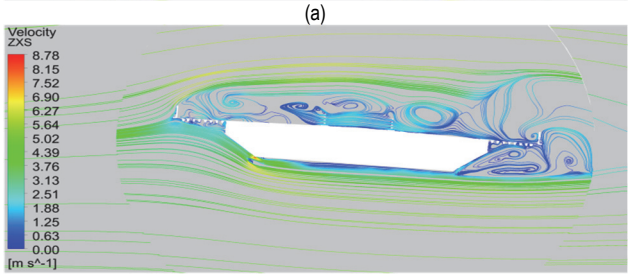

(b)

Figure 17 Instantaneous streamline diagram of T for +5° wind attack angle section: a). original-ZX section; b) F1K2-ZX cross-section

Fig. 18 shows the distribution of vorticity for the ZX section of the straight web plate steel box beam with outer guardrail expansion measures applied at +5° wind attack angle. By comparing the vorticity distribution diagrams of the original section and F1K2-ZX section, it can be observed that after the measures are applied, the first clockwise vortex of the wake rotates approximately 0.55*B* and the counterclockwise vortex rotates 0.62*B*, corresponding to a decrease of 54.2% and 8.8% in the lengths of the first vortex shedding in the wind direction of the original section, respectively. Furthermore, the range of strong vortices in the wake area is reduced to 3.89*B* –4.27*B*, with an average length reduction of 41.5%. This indicates that the outer guardrail F1K2 measures effectively reduce the energy of the spanwise vortices, resulting in reduced effects on the structure from the vortices shedding under the same wind speed conditions. The overall effect of the wake field on the structure is also reduced, and the phenomenon of vortex-induced vibration is effectively suppressed.

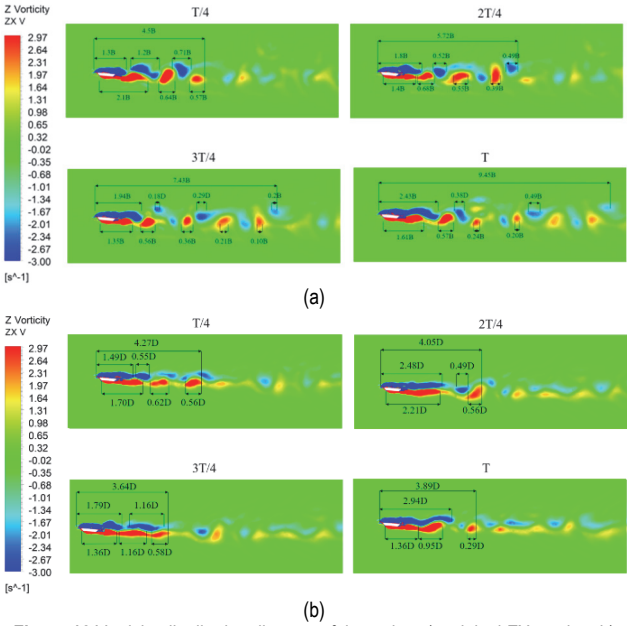

Figure 18 Vorticity distribution diagram of the wake: a). original-ZX section; b) F1K2-ZX cross-section

By comparing the shedding lengths of the vortices, it was observed that the installation of a wind fence results in an extended wake downstream of the structure, causing a backward shift of the von Karman vortices along the cross-deck direction. Due to the mass of air surrounding the deck being included in the vibration of the structure, the elongated wake caused by the wind fence leads to an increased mass contribution to the overall vibration of the structure. Additionally, the shifted shedding of the von Karman vortices reduces the force exerted on the main beam. Consequently, the amplitude of the vibration of deck is reduced.

3.2.3 Surface Forces

To explain the effectiveness of aerodynamic measures from a structural force perspective, Fig. 19 shows the upper surface pressure distribution on the original cross-section and the main beam cross-section under the F1K2 arrangement for a +5° wind attack angle. At $t = T/4$, the vortex downstream of the main beam develops noticeably and has not completely detached. At this moment, negative pressure acts on all bridge panels, as evident from the black box in Fig. 19a at $T/4$, showing a decrease in negative pressure near the downstream bridge panel. At $t = 2T/4$, the upper-side vortex detaches from the main beam, but the isosurface of the vorticity exhibits discontinuities in the spanwise direction, indicating significant disruption to the spanwise structure of the vortex after passing over the complex aerodynamic shape of the upper surface. Combined with the instantaneous streamline map, it can be inferred that due to the negative pressure near the railing of the upstream bridge panel, the main flow exhibits a significant downward inclination. Therefore, at high wind attack angles, the vortex structure is more severely affected by the enclosed section downstream of the railing. In comparison, the open section has a smaller wind-facing area and a certain level of air permeability, which helps maintain the vortex structure. In the enclosed section, the negative pressure is greater near the upstream position of the bridge panel, resulting in a more pronounced downward inclination of the main flow. After being squeezed by the main flow, the vortex moves closer to the wall surface, and its influence range expands due to the frictional effect of the wall and the obstruction of the railing, leading to energy dissipation. The relationship between the vortex motion at $3T/4$ and T and the force distribution on the structural surface can be similarly explained.

3.3 Effect of the Enclosed Railing

The wake vortex near the structure has the significant impact on the main beam. Therefore, monitoring data at a spanwise position 0.2*B* from the lower edge of the structure is selected for polynomial trend fitting to compare the effects of the two measures based on the wake flow parameters and explain the reasons. The same phenomenon was observed by using the CFD simulation in a numerical wind tunnel.

As shown in Fig. 20, under +5° wind attack angle, the spanwise distribution trends of the wind speeds for the two measures are the same, and the overall wind speed values for the F1K2 railing arrangement are higher than those for the F1K3 arrangement. At +3° wind attack angle, the wind speed distribution trends for the three scenarios are similar, but the peak wind speed at the wake measurement point decreases after implementing the aerodynamic measures.

Regarding vorticity, based on the above analysis, the rotational component around the *Z*-axis is the primary cause of structural vibration. Under the +5° wind attack angle, the original cross-section exhibits clockwise rotating vortices at the measurement points, and the vortices have high energy, indicating that their aerodynamic forces on the structure in the vertical direction have the same direction and relatively large magnitude. With the F1K2 railing arrangement, significant changes occur in the vortices at the position corresponding to the right column of the 4th railing, where the rotation directions are opposite on both sides, and the magnitudes of the peak vorticities are relatively close. This indicates a sudden change in the

aerodynamic forces of the vortices on the structure in the vertical direction, resulting in a smaller net aerodynamic force. With the F1K3 railing arrangement, the overall vortex energy decreases, and the vortices in the range of measurement points corresponding to the 2nd and 3rd railings exhibit smaller clockwise rotations. Consequently, the net aerodynamic force on the structure in the vertical direction also decreases, leading to a suppression effect on the vertical bending vibration of the model.

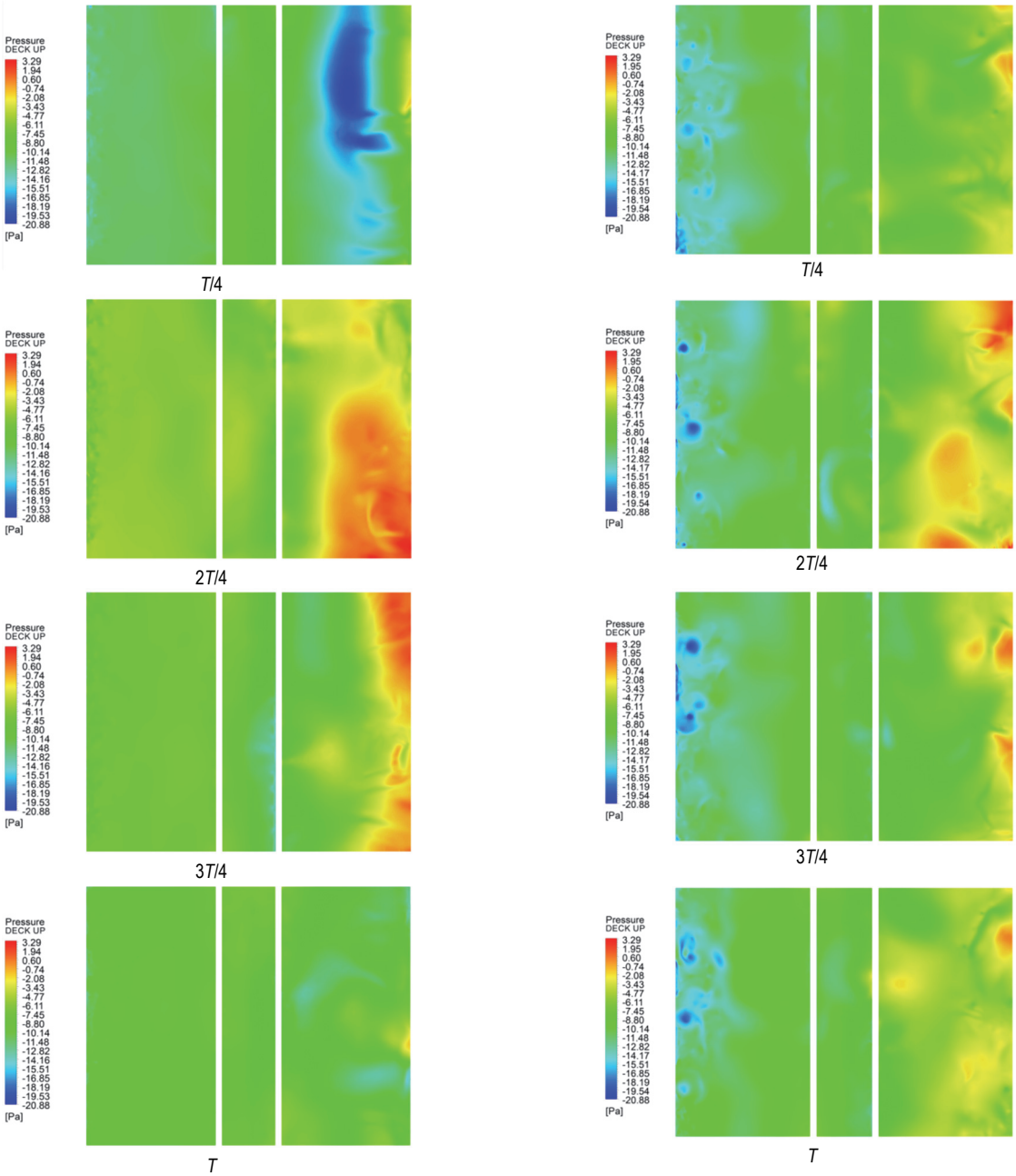

Figure 19 Pressure distribution map on the main beam cross-section: a). original-ZX section; b) F1K2-ZX cross-section

At +3° wind attack angle, the main cross-section predominantly exhibits counterclockwise rotating vortices, with smaller clockwise vortices occurring at the measurement points corresponding to the 7th - 8th and 10th - 11th railings. Although the rotational directions are the same for the F1K2 measure, the magnitude of the spanwise vorticity is significantly reduced, resulting in a weaker influence of the wake on the structure and a certain degree of suppression of main beam vibration. With the F1K3 measure, notable changes occur in the wake vortices near the structure compared to the original cross-section, with completely opposite rotational directions and similar magnitudes of the peak vorticities.

By comparing and analyzing the flow field information at the 0.2*B* position in the wake region, the following conclusions can be drawn: in terms of velocity, the F1K3 arrangement results in the smallest reduction in the wake velocity, and the spanwise distribution trends of the wind speeds are similar for both measures. From the perspective of spanwise vorticity, the F1K2 arrangement exhibits more distinct differences in vortex rotation directions as illustrated in Fig. 20 in the spanwise direction, indicating a better suppression effect.

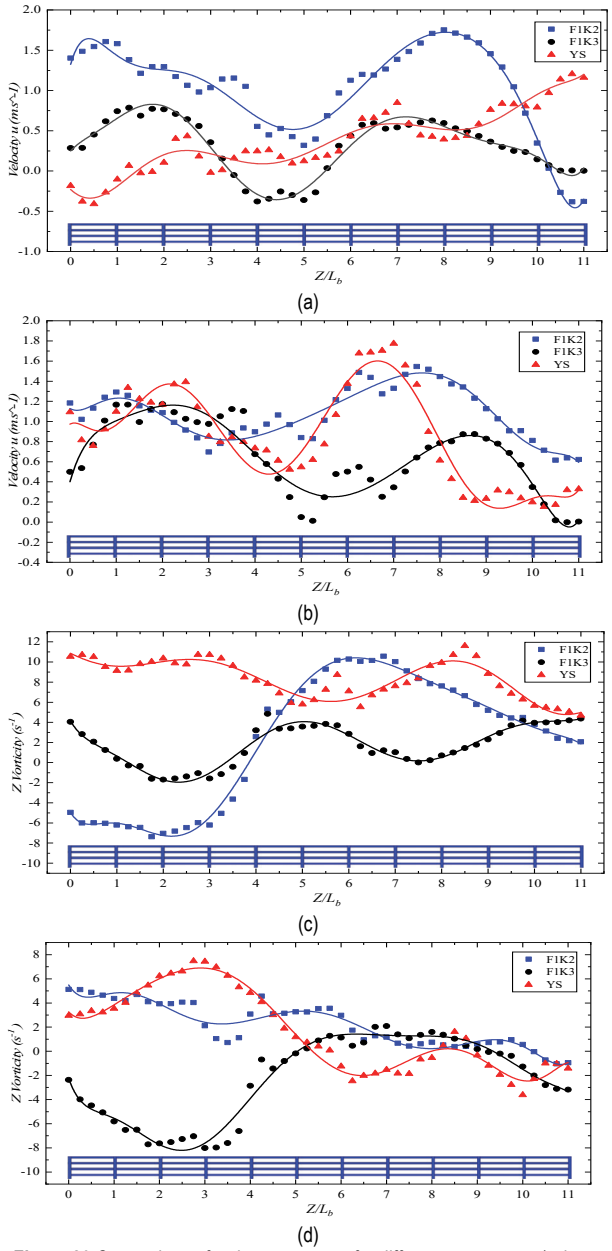

Figure 20 Comparison of wake parameters for different measures: a) along-wind velocity distribution (+5° wind angle of attack); a) along-wind velocity distribution (+3° wind angle of attack); c) Z-directional vorticity distribution (+5° wind angle of attack); d) Z-directional vorticity distribution (+3° wind angle of attack)

Fig. 21 shows the pressure distribution cloud map at the bridge deck location under F1K3 measures and a wind angle of attack of +5°. The pressure cloud map under F1K2 measures can be seen in Fig. 14b. To facilitate comparison, the cloud map threshold is set to the same as the corresponding original cross-section operating condition (–20.88 Pa to –3.29 Pa). The airflow's vertical forces on the main beam are closely related to its vertical bending vibration. From the pressure distribution on the bridge deck in the original cross-section shown in Fig. 14, it can be observed that when the model undergoes vortex-induced vibration, there are significant positive and negative pressure variations at the downstream bridge deck location, indicating the significant effect of wake vortex shedding. After the installation of longitudinal closed barriers, there are significant changes in the pressure distribution on the bridge deck during one cycle. The clear alternation of positive and negative pressures at the downstream bridge deck is no longer evident, indicating the suppression of the wake vortex's effect.

Under F1K2 measures, the upstream bridge deck exhibits a strong negative pressure zone throughout the cycle, corresponding to the area behind the closed section of the barrier. The downstream bridge deck shows alternating positive and negative pressures during one cycle, but the correlation of pressure distribution along the span decreases. Positive pressures are observed near the downstream bridge deck at $T/4$, $T/2$, and $3T/4$ moments, with the maximum value occurring at $T/2$, which is 5.75 Pa.

Under F1K3 measures, the main beam bridge deck is predominantly characterized by negative pressure distribution throughout the cycle, with only a peak positive pressure of 1.11 Pa occurring at the downstream location during $T/4$ moment. Due to the increased spacing between closed barrier sections, the negative pressure behind the upstream barrier diminishes, and the larger spacing of the closed sections causes significant spanwise deformation of the airflow after transition, resulting in weakened negative pressure and downstream movement. At the same cloud map threshold, the negative pressure on the downstream bridge deck throughout the cycle is larger under F1K3 measures compared to F1K2 measures.

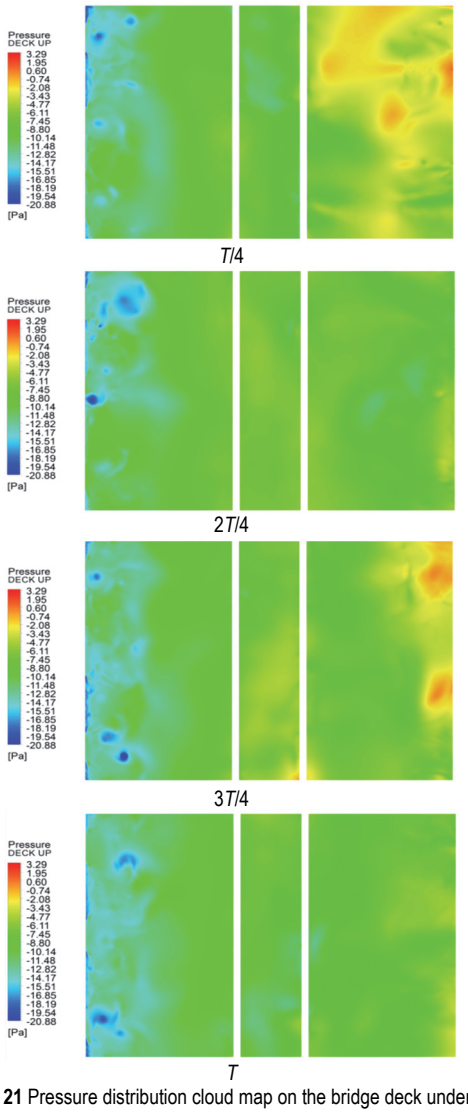

Figure 21 Pressure distribution cloud map on the bridge deck under F1K3 measures

The wake vorticity distribution in the wake region under F1K3 measures is shown in Fig. 22. The first vortex shedding length scales for the along-wind direction are 1.19*B* and 0.55*B* in a clockwise and counterclockwise rotation, respectively. These values are close to the first vortex shedding length scales for the original cross-section operating condition (1.2*B*, 0.68*B*). The range of strong vortices under F1K3 measures is from 3.28*B* to 3.59*B*, with an average length reduction of 49% compared to the original cross-section, and a more significant reduction compared to the effects of F1K2 measures. This indicates that the energy of the first vortex shedding in the spanwise direction is the lowest under F1K3 measures, resulting in decreased structural effects and reduced structural vibration.

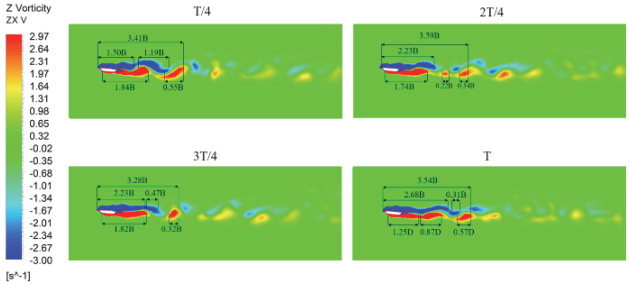

Figure 22 Wake vorticity distribution on the F1K3-ZX cross-section (+5° wind angle of attack)

4 DISCUSSION

Through large-eddy simulation (LES) numerical analysis of the straight diaphragm steel box girder cross-section under the original condition and two aerodynamic measures, in-depth research has been conducted on the bridge cross-section's vibration and the damping effects of aerodynamic measures from the perspectives of flow field around the structure and structural forces. The following conclusions have been drawn:

(1) The aerodynamic shape of the straight diaphragm steel box girder cross-section exhibits small spanwise differences. When the flow passes through the upstream barrier, the vortex structures at various barrier positions are relatively similar, with predominance of along-wind vortices rotating around the *Z*-axis. The flow velocity accelerates when passing through the unobstructed section, and the flow near the lower position forms significant vortices within the negative pressure zone formed by the bridge deck and the curb, gradually developing and being engulfed by the large-scale vortices generated at the upstream bridge deck due to wall viscous forces. When the wind angle of attack is large (+5° wind angle of attack), the model itself has a large height difference in the flow direction, causing minimal disturbance to the vortices generated at the upstream bridge deck due to the presence of the central crash barrier. Consequently, the vortices shed downstream have larger sizes and energies, resulting in greater vibration amplitudes compared to a +3° wind angle of attack.

(2) When the outer side of the closed barrier is considered, a significant negative pressure zone appears on the windward side of the upstream bridge deck, resulting in a large spanwise component of the along-wind flow and evident three-dimensional vortex characteristics. The energy of along-wind vortices is reduced. Under the negative pressure effect on the bridge deck, the upper part of the boundary layer tilts downward toward the main beam surface, causing faster dissipation of vortices at various positions on the upper surface, reducing the size and energy of wake vortices, and suppressing structural vibration.

(3) The damping mechanisms of the two measures are different. Under F1K2 measures, there is a strong negative pressure zone upstream on the bridge deck, located higher, which causes a significant spanwise component and dissipation of surface vortices due to the downstream inclination of the main flow, resulting in a reduction in the size and energy of the first vortex shedding in the along-wind direction. The spanwise rotation direction and three-dimensional characteristics of the wake structure are evident. Under F1K3 measures, the upstream bridge deck exhibits weaker negative pressure and is positioned further downstream. Although it has little effect on the flow direction and the size of the first vortex shedding in the along-wind direction, and the three-dimensional characteristics of the wake structure are weaker compared to F1K2 measures, the energy of wake vortices is low, and the range of strong vortices is minimal, leading to a decrease in pressure difference between the upper and lower surfaces of the structure.

Acknowledgements

This study is funded by the National Key R&D Program of China (Grant Number: 2021YFB2600600); Henan Province Science and Technology Research Project (242102240035).

5 REFERENCES

[1] Laima, S. J., Li, H., Chen, W., & Jinping, O. (2018). Effects of attachments on aerodynamic characteristics and vortex-induced vibration of twin-box girder. *Journal of Fluids and Structures*, *77*, 115-133. https://doi.org/10.1016/j.jfluidstructs.2017.12.005

[2] Wang, Y. X. (2023). Experimental study on the influence of railing structure on vortex-induced vibration performance of streamlined box girder. *Shijiazhuang Tiedao University.*

[3] Liu, Q. K., Wang, Y. X., Sun, Y. F. et al. (2023). Experimental study on influence of railings heights on vortex-induced vibration performance of streamlined box girder. *Journal of Hunan University (Natural Science Edition)*, *50*(07), 140-150.

[4] Li, C. G., Zhang, J., Han, Y. et al. (2019). Mechanism of the influence of railing cornerstone on vortex-induced vibration of closed box girder bridge. *China Journal of Highway and Transport*, *32*(10), 150-157.

[5] Cui, X., Wang, H. X., Guan, Q. H. et al. (2018). Wind tunnel experimental on influence of railing ventilation rate oncharacteristics of vortex-induced vibration of main girder. *Journal of Chang 'an University (Natural Science Edition)*, *38*(03), 71-79.

[6] Li, M., Sun, Y. G., Li, M. S. et al. (2018). Vortex-induced vibration performance of wide streamlined box girder and aerodynamic countermeasure research. *Journal of Southwest Jiaotong University*, 53, *242*(04), 56-63.

[7] Cao, F. C., Ge, Y. J., Wu, T. (2007). Research on Vortex-induced Resonance and Aerodynamic Control Measures of Steel Box Girder Cable-stayed Bridge. *Wind Engineering Committee of Bridge and Structural Engineering Branch of*

China Civil Engineering Society. Proceedings of the 13th National Symposium on Structural Wind Engineering, 1(6).

[8] Li, K. W., Sun, Y. F., Hu, B. et al. (2023). Experimental study on the influence of close state of railing on vortex-induced viberation characteristics of streamlined box girders.*Structural Engineering Committee of Chinese Society of Mechanics, Jiangxi University of Science and Technology, Engineering Mechanics Editorial Committee of Chinese Society of Mechanics, Civil Engineering Department of Tsinghua University, State Key Laboratory of Water and Sediment Science and Water Conservancy and Hydropower Engineering (Tsinghua University). Proceedings of the 32 nd National Conference on Structural Engineering*, *2*(5).

[9] Yang, S. Q. (2023). Wind tunnel test study on the influence of railing ventilation rate on vortex-induced vibration characteristics of central slotted box girder. *China Association for Science and Technology, Ministry of Transport, Chinese Academy of Engineering, Hubei Provincial People 's Government.2023 World Transportation Conference (WTC2023) Proceedings (Volume I). People 's Transportation Publishing House Co., Ltd., 5*.

[10] Li, M., Sun, Y., Jing, H., & Li, M. (2018). Vortex-Induced Vibration Optimization of a Wide Streamline Box Girder by Wind Tunnel Test. *KSCE J Civ Eng, 22*, 5143-5153. https://doi.org/10.1007/s12205-018-0548-y

[11] Evangelinos, C. (1999). Parallel simulations of vortex-induced vibrations in turbulent flow: Linear and nonlinear models. *Dissertation Abstracts International.*

[12] Murakami, S. (1992). Numerical study on velocity-pressure field and wind forces for bluff bodies by k-ε, ASM and LES. *Journal of Wind Engineering and Industrial Aerodynamics*, *44*, 2841-2852. https://doi.org/10.1016/0167-6105(92)90079-P.

[13] Ke, J. (2019). RANS and hybrid LES/RANS simulations of flow over a square cylinder. *Advances in Aerodynamics*, *1*(1), 10. https://doi.org/10.1186/s42774-019-0012-9

[14] Altland, S., Xu, H. H. A., Yang, X. I. A., & Robert, K. (2021). Modeling of Cube Array Roughness: RANS, LES, and DNS. *Fluids Engineering Division Summer Meeting. American Society of Mechanical Engineer*s, 85307: V003T05A027. https://doi.org/10.1115/1.4053611

[15] Selvam, R. P. (1993). Finite element modeling of flow around circular cylinder using LES. *Journal of Wind Engineering and Industrial Aerodynamics*, *36,* 129-139. https://doi.org/10.1016/S0167-6105(97)00068-8

[16] Tunstall, R., Laurence, D., Prosser, R., & Skillen, A. (2017). Towards a generalised dual-mesh hybrid LES/RANS framework with improved consistency. *Computers & Fluids*, *157*, 73-83. https://doi.org/10.1016/j.compfluid.2017.08.002

[17] Tamura, T. (1993). On the reliability of two-dimensional simulation for unsteady flows around a cylinder-type structure. *Journal of Wind Engineering and Industrial Aerodynamic*, *35*, 275-298. https://doi.org/10.1016/0167-6105(90)90221-W

[18] Zhang, L. L., Wu, B., Yang, Y., et al. (2016). Effects of subsidiary members and deck surface roughness on the aerodynamic coefficients of static forces on a flat box girder. *Experimental fluid dynamics*, *129*(01), 76-82.

[19] Jiang, T. H. (2009). Control for wind-induced vibration responses of long-span bridge. *Wuhan University of Technology*. https://doi.org/10.7666/d.y1559740

Contact information:

Sai GONG
School of Highway,
Chang'an University,
Xi'an710064, Shaanxi, China,
Nanyang Institute of Technology,
Nanyang 473004, Henan, China;

Xue ZHAO
School of Highway,
Chang'an University,
Xi'an710064, Shaanxi, China

Shucheng YANG
(Corresponding author)
School of Highway,
Chang'an University,
Xi'an710064, Shaanxi, China
Email: syang325@chd.edu.cn